Journal of Sound and Vibration (2001) **247**(3), 471–487
doi:10.1006/jsvi.2001.3767, available online at http://www.idealibrary.com on IDEAL®

PARAMETER STUDIES FOR PLANE STRESS IN-PLANE VIBRATION OF RECTANGULAR PLATES

K. Hyde, J. Y. Chang, C. Bacca and J. A. Wickert

Department of Mechanical Engineering, Carnegie Mellon University, Pittsburgh, PA 15213 *U.S.A.*

(*Received* 2 *November* 2000, *and in final form* 13 *April* 2001)

Free in-plane vibration of rectangular plates undergoing plane stress deformation is investigated through Ritz discretization of the Rayleigh quotient. Of particular interest is the manner in which the plate's natural frequencies and coupled longitudinal–lateral vibration modes evolve as its length-to-width aspect ratio is varied. Vibration modes are grouped into families or classes based on (1) common asymptotic behavior of natural frequency loci with increasing aspect ratio, (2) reflective symmetry of the displacement field about the plate's centerline, and (3) the presence of nodal points on or off the plate's centerline. The applicability of the traditional strength-of-materials bending and longitudinal vibration models for predicting the lower in-plane modes is also discussed, and the range of aspect ratios for which those simpler models provide acceptable accuracy is quantified. In-plane twisting and higher order modes having nodal points off the plate's centerline are not predicted by those traditional theories, and these are also discussed in several parameter studies.

1. INTRODUCTION

Because of the higher strain energy involved in their deformations, in-plane vibration of plates generally occurs at substantially higher frequencies than transverse vibration. In certain specialized applications, however, in-plane vibration can be of interest despite the higher frequencies involved. In magnetic tape data storage, transverse vibration is generally not an issue in path design, but in-plane vibration occurring in the kilohertz range does have implications for actuation of the recording heads in following narrow data tracks. Also with respect to the transportation of webs, such other materials as flexible strips of polymer, film, sheet metal, and paper are positioned during their production by cylindrical guides and rollers. For an aluminum sheet in a rolling mill, in-plane vibration influences the web's surface condition at those web–roller interactions. Objectives of this investigation include examining the manner in which the in-plane modes vary with plate's aspect ratio, and assessing the accuracy and limitations of the traditional strength-of-materials theories which are often used to estimate the natural frequencies.

Previous studies in the area of in-plane vibration include work by Handa [1], who developed a new type of element for use in modelling the vibration of such plate-type structures as the shear walls used in building construction. The element developed had more degrees of freedom per node than previously used ones, and thus was able to facilitate frequency and mode shape computation with greater accuracy. Also, with a view towards computational techniques, Ovunc [2] applied the continuous mass matrix method and presented free and forced response results for the cases of a cantilever, and of a plate having all edges constrained. Results were presented only for those boundary conditions and

0022-460X/01/430471 + 17 $35.00/0

several specific values of the plate's aspect ratio. Kobayashi *et al.* [3] treated the in-plane vibration of rectangular plates that are supported at four interior points, and examined the variation of frequencies and mode shapes with respect to the locations of those supports. The Lagrange multiplier technique was applied to constrain the plate's displacements at the supports. Liew *et al.* [4–7] examined the three-dimensional vibration of rectangular parallelepipeds and plates having arbitrary thickness through the Rayleigh–Ritz method. Tabular data for the natural frequencies of certain symmetric and antisymmetric modes were presented for various combinations of free and constrained boundary conditions, and as functions of the plate's thickness or parallelepiped's aspect ratio.

Bardell *et al.* [8] studied the in-plane vibration of isotropic rectangular plates having either free or fully constrained boundaries, and results were presented for the lower six modes at two particular aspect ratios. The classification of groups of modes having natural frequencies with qualitatively similar behavior as the aspect ratio is varied was not discussed. Larsson [9] later described detailed experimental results obtained through in-plane modal testing of an aluminum plate. For a length-to-width aspect ratio of 2·08, measured and predicted results for the first 15 mode shapes were presented, and those measurements can provide a valuable benchmark for verifying results predicted through analytical techniques.

In this paper, the natural frequency spectrum and vibration modes for in-plane vibration of isotropic rectangular plates undergoing plane stress deformation is investigated. For three prototypical sets of boundary conditions—free, constrained–free, and constrained—natural frequencies and modes shapes are obtained through Ritz discretization of the Rayleigh quotient. The results obtained for the free, and for the constrained–free, geometries are discussed and compared with those obtained from the traditional strength-of-materials theories for bending and longitudinal vibration. Adding to the findings of previous investigations, natural frequency results are depicted here over a wide range of aspect ratios in order to examine the asymptotic behavior of the different classes of modes. The ranges of aspect ratios over which the simpler theories can be applied with fidelity to the problem at hand are quantified, and other classes of modes that are not predicted within the context of the traditional theories are also identified in the case studies.

2. IN-PLANE VIBRATION MODEL AND DISCRETIZATION

A rectangular plate of length a along the x-axis, width b across the y-axis, and thickness $h \ll a$ and b is examined, where the co-ordinate system is located centrally within the plate. Only in-plane, plane stress vibration is treated so that all loads act within the plane of the plate, stress components σ_z, τ_{xz}, and τ_{yz} each vanish, and stresses σ_x, σ_y, and τ_{xy} do not vary across the plate's thickness and are at most functions only of the in-plane co-ordinates. The material is specified to be isotropic with modulus E, the Poisson ratio ν, and volumetric mass density ρ.

In-plane displacements along the x and y directions are denoted by $u(x, y, t)$ and $v(x, y, t)$, respectively, and in terms of them, the kinetic T and potential V energies are

$$T = \frac{\rho h}{2} \int_{-b/2}^{b/2} \int_{-a/2}^{a/2} ((u_{,t})^2 + (v_{,t})^2)\, \mathrm{d}x\, \mathrm{d}y, \tag{1}$$

$$V = \frac{Eh}{2(1-\nu^2)} \int_{-b/2}^{b/2} \int_{-a/2}^{a/2} (u_{,x}^2 + 2\nu u_{,x} v_{,y} + v_{,y}^2 + (1-\nu)(u_{,y} + v_{,x})^2/2)\, \mathrm{d}x\, \mathrm{d}y, \tag{2}$$

where the comma-subscript notation signifies partial differentiation. Through standard application of Hamilton's principle

$$\delta \int_{t_1}^{t_2} (T - V)\,\mathrm{d}t = 0, \tag{3}$$

the equations of motion for coupled u–v motions become

$$\rho\ddot{u} - \frac{E}{1-\nu^2}(u_{,xx} + \nu v_{,xy}) - \frac{E}{2(1+\nu)}(u_{,yy} + v_{,xy}) = 0,$$

$$\rho\ddot{v} - \frac{E}{1-\nu^2}(v_{,yy} + \nu u_{,xy}) - \frac{E}{2(1+\nu)}(v_{,xx} + u_{,xy}) = 0. \tag{4}$$

With the definition of the state vector $\underline{w} = \{uv\}^{\mathrm{T}}$, 2×2 mass operator $\underline{\mathscr{M}} = Diag(\rho h)$, and stiffness operator

$$\underline{\mathscr{K}} = -\frac{Eh}{1-\nu^2}\begin{bmatrix} \dfrac{\partial^2}{\partial x^2} + \dfrac{1-\nu}{2}\dfrac{\partial^2}{\partial y^2} & \dfrac{1+\nu}{2}\dfrac{\partial^2}{\partial x \partial y} \\ \dfrac{1+\nu}{2}\dfrac{\partial^2}{\partial x \partial y} & \dfrac{\partial^2}{\partial y^2} + \dfrac{1-\nu}{2}\dfrac{\partial^2}{\partial x^2} \end{bmatrix}, \tag{5}$$

the equations of motion are compactly written in the symbolic operator form $\underline{\mathscr{M}}\underline{w}_{,tt} + \underline{\mathscr{K}}\underline{w} = \underline{0}$. Here the underline notation signifies either a vector or matrix quantity.

On the plate's transverse edges $x = \pm a/2$, the two conditions which must be satisfied are $\sigma_x \delta u = 0$ and $\tau_{xy}\delta v = 0$. Likewise, on the longitudinal edges $y = \pm b/2$, $\sigma_y \delta v = \tau_{xy}\delta u = 0$. Here σ_x and σ_y denote the normal stresses in the x and y directions, τ_{xy} is the shear stress, and δu and δv denote admissible infinitesimal variations in u and v. On each edge of the boundary, either a certain stress component or the variation of a certain displacement vanishes, and in what follows, various combinations of free and ideally constrained edges are considered. The term "clamped", as is used, for instance, in examining transverse vibration in the traditional beam and plate theories, is specifically avoided since its usage implies the imposition of different boundary condition expressions on only one variable.

The model is non-dimensionalized through the definitions

$$x' = x/a, \qquad y' = y/b, \qquad u' = u/a, \qquad v' = v/b, \qquad t' = t/\sqrt{\rho/Ea^2}, \tag{6}$$

and in what follows, the prime superscripts are omitted for brevity. To determine the natural frequencies and vibration modes, the model is discretized globally through the Rayleigh–Ritz method. With harmonic time dependence specified, and in terms of the spatial components $\underline{w}_o = \{u_o\, v_o\}^{\mathrm{T}}$ only of the continuous displacement field, Rayleigh's quotient becomes

$$\mathscr{R} = \frac{\langle \underline{\mathscr{K}}\underline{w}_o, \underline{w}_o \rangle}{\langle \underline{\mathscr{M}}\underline{w}_o, \underline{w}_o \rangle}, \tag{7}$$

where the nomenclature $\langle \bullet, \bullet \rangle$ denotes the conventional inner product, and the order of derivatives on u and v has been lowered in the numerator following application of Green's

theorem. The displacements in turn are approximated by the NW-term expansions

$$u_o \approx u_o^{NW} = \underline{c}^{\mathrm{T}}\underline{\phi}, \qquad v_o \approx v_o^{NW} = \underline{d}^{\mathrm{T}}\underline{\psi}, \tag{8}$$

with generalized co-ordinates c_i and d_j, and admissible functions ϕ_i and ψ_j. Vectors $\underline{c}$, $\underline{d}$, $\underline{\phi}$, and $\underline{\psi}$ are each of length NW. Each ϕ_i or ψ_j is constructed from separable components in x and y, for instance $\phi_i = X_n(x)Y_m(y)$, with indices m and n being related to i by $m = i - \mathrm{Trc}((i-1)/N)N$ and $n = 1 + \mathrm{Trc}((i-1)/N)$. Here the function "Trc" truncates its operand to the next lowest integer, and N is the integer closest to $\sqrt{NW}$. The ψ_j are developed similarly, but potentially with different $X_n(x)$ and $Y_m(y)$ in order to satisfy the boundary condition requirements. With opposing edges being fully constrained, sinusoids are used as the set of admissible functions, and Legendre polynomials are used when the opposing edges are free.

For a chosen value of NW, matrices $\underline{K}$ and $\underline{M}$ of dimensions $2NW \times 2NW$ are formed from the $\mathscr{M}$ and $\mathscr{K}$ weighted projections of $\{u_o^{NW}\ v_o^{NW}\}^{\mathrm{T}}$ as in equation (7). The eigenvalue problem $\underline{K}_{\underline{q}} = \omega^2 \underline{M}_{\underline{q}}$ is obtained, where the generalized co-ordinate vector is given by $\underline{q} = \{\underline{c}\ \underline{d}\}^{\mathrm{T}}$, in order to provide discrete approximations to the dimensional natural frequencies $\omega = \omega/(E/\rho a^2(1-\nu^2))^{1/2}$ and to the coupled u–v mode shapes as reconstructed from equation (8).

3. NATURAL FREQUENCY AND MODE STRUCTURE

Natural frequency and mode shapes are presented in the following sections for three combinations of edge conditions: free, opposing pairs being constrained or free, and constrained. In each case, the first 20 natural frequencies were calculated and relative convergence was reached at $NW = 110$, 100, and 80 in the three cases respectively.

To benchmark accuracy of the method, natural frequencies for plates having either free or constrained boundaries were compared with results obtained by Bardell *et al.* [8] for the aspect ratios $a/b = 1{\cdot}0$ and $2{\cdot}0$. Those comparisons are shown in Tables 1 and 2, where deviations are less than 2% over the first six modes, and over four combinations of boundary conditions and aspect ratios.

Results for higher frequency modes were not reported in reference [8], but measured values for the first 15 in-plane modes of a thin, free, aluminum plate having aspect ratio 2·08

TABLE 1

Comparison of the present predicted non-dimensional natural frequencies ω^* with results reported by Bardell et al. [8]; *free boundary*

$a/b = 1{\cdot}0$			$a/b = 2{\cdot}0$		
ω^*	Bardell [8]	Difference (%)	ω^*	Bardell [8]	Difference (%)
2·301	2·321	0·9	1·938	1·954	0·8
2·471	2·472	0·1	2·927	2·961	1·2
2·471	2·472	0·1	3·238	3·267	0·9
2·589	2·628	1·5	4·702	4·726	0·5
2·971	2·987	0·5	4·752	4·784	0·7
3·501	3·452	1·4	5·178	5·205	0·5

TABLE 2

Comparison of the present predicted non-dimensional natural frequencies ω^* with results reported by Bardell et al. [8]; *constrained boundary*

$a/b = 1{\cdot}0$			$a/b = 2{\cdot}0$		
ω^*	Bardell [8]	Difference (%)	ω^*	Bardell [8]	Difference (%)
3·549	3·555	0·2	4·741	4·789	1·0
3·549	3·555	0·2	6·387	6·379	0·1
4·221	4·235	0·3	6·682	6·712	0·5
5·201	5·186	0·3	7·037	7·049	0·2
5·967	5·859	1·8	7·565	7·608	0·6
6·000	5·895	1·8	8·128	8·140	0·2

TABLE 3

Comparison of the present predicted natural frequencies (ω^* and $\omega/2\pi$) with the measured values reported by Larsson [9] *for a free aluminum plate*; $E = 70{\cdot}3$ GPa, $\nu = 0{\cdot}33$, $\rho = 2674$ kg/m^3, $a = 1{\cdot}023$ m, $b = 0{\cdot}493$ m, *and* $h = 9{\cdot}7$ mm

Mode	ω^*	$\omega/2\pi$ (Hz)	Larsson [9] (Hz)	Difference (%)
1	1·903	1608	1603	0·3
2	2·931	2477	2472	0·2
3	3·272	2765	2740	0·9
4	4·749	4014	3959	1·4
5	4·800	4057	4008	1·2
6	5·275	4459	4424	0·6
7	5·405	4568	4503	1·4
8	5·555	4695	4628	1·5
9	6·325	5346	5269	1·5
10	6·528	5517	5376	2·6
11	6·778	5728	5659	1·2
12	6·894	5826	5737	1·6
13	6·942	5867	5812	1·0
14	7·637	6455	6287	2·7
15	8·184	6917	6655	3·9

were reported by Larsson [9]. That comparison, which is made in dimensional terms in order to be consistent with the presentation of reference [9], is shown in Table 3. The present results agree within 4% over the first 15 modes, and for 12 of the listed values, the correlation is within 2%. Results were not presented in reference [9] for plates with any other aspect ratio or boundary conditions.

The in-plane mode shapes involve coupled u–v motions and are classified for purposes of exposition according to symmetry of the two displacement components. The vibration modes are termed either symmetric or antisymmetric with respect to $y = 0$, consistent with the convention of reflective symmetry about the plate's longitudinal centerline. In a symmetric mode shape S, u and v are even and odd functions, respectively, of the transverse co-ordinate y; the converse is valid for an antisymmetric shape A. The in-plane modes are further classified according to the number and placement of nodes in x and

y relative to the $y = 0$ centerline. The so-called first order modes have nodal points $u = v = 0$ only on the centerline's axis, whereas higher order modes can also have off-axis nodes.

4. FREE BOUNDARY

Figure 1 depicts the dimensionless in-plane natural frequency spectrum for a free plate. The frequency loci are shown over aspect ratios $1 < a/b < 10$. The predicted values (solid line type) are compared to the frequencies predicted on the basis of the classical Euler–Bernoulli beam bending (dashed line type) and longitudinal rod (arrows on ordinate) theories for larger a/b.

4.1. IN-PLANE BENDING MODES

The loci in Figure 1 for one class of modes decrease gradually with a/b for larger aspect ratios. The mode labelled (i) in Figure 1 is representative and is the second lowest of this class. Such vibration modes are analogous to conventional beam bending modes in terms of their u–v displacement patterns and the asymptotic behavior of their natural frequencies with a/b. Mode (i), depicted in Figure 2, is an antisymmetric mode, analogous to the second

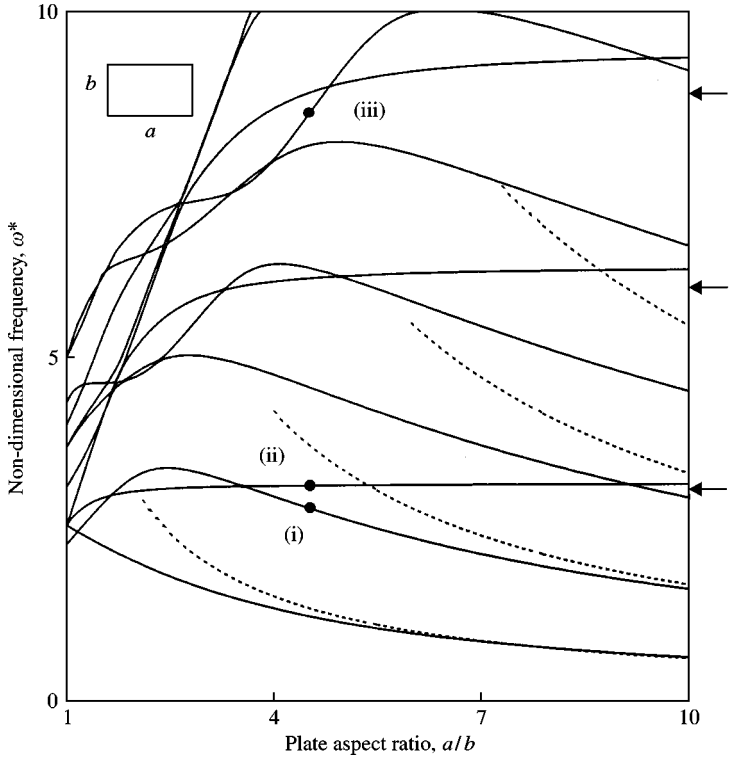

Figure 1. Non-dimensional frequency spectrum (solid line type) for in-plane vibration of a free plate shown as a function of aspect ratio. The frequencies predicted through traditional beam bending (dashed line type) and longitudinal rod (arrows on ordinate) theories are shown for comparison at larger aspect ratios. The frequencies of modes (i)–(iii), depicted in Figures 2–4, are indicated by the "●" notation.

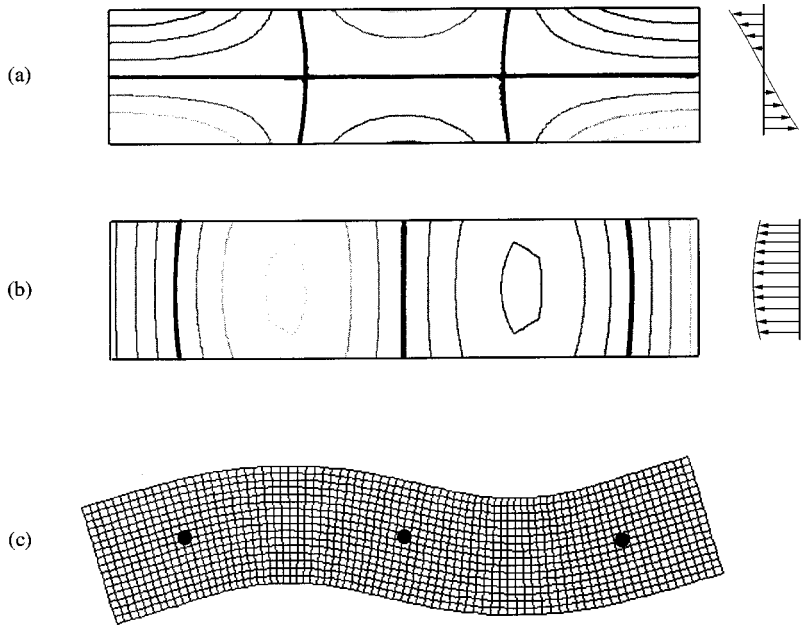

Figure 2. Second in-plane bending mode, labelled (i) in Figure 1, for a free plate at $a/b = 4{\cdot}5$; $\omega = 2{\cdot}80$, antisymmetric. (a) Longitudinal displacement contour and its lateral profile, (b) lateral displacement contour and its lateral profile, and (c) deformed shape with "●" notation signifying nodal points. The nodal lines in (a) and (b) are highlighted in bold.

mode of a free–free beam, with motion occurring predominately in v. The longitudinal displacement varies in a substantially linear manner with y, as seen in Figure 2(a), and the v profile of Figure 2(b) has only a slight roll-off near the edges.

In the limit $a/b \to \infty$, the vibration modes in this class tend to those expected on the basis of beam bending theory. In that case, with a and b interpreted as the beam's length and depth, ω decreases as $1/a^2$ and the non-dimensional value ω^* varies with $(a/b)^{-1}$ as indicated by the loci with dashed line type in Figure 1. For aspect ratios greater than roughly 5·5, for instance, the frequency of the lowest in-plane mode in this class is within 5% of the value predicted through beam bending theory. For aspect ratios greater than 8·0, the simpler theory is accurate to within 9% of the value predicted for the second mode of this class, mode (i).

Nodes form at the intersection of nodal lines in the u and v contours. For the case of mode (i), all nodes lie on the centerline, and as a result, mode (i) is classified as a first order mode. The nth mode of this class characteristically has $n + 1$ centerline nodes. Nodes in Figure 2(c) form where the longitudinally oriented nodal line for u intersects the transverse nodal lines in v. In this case, the number of nodal lines for v oriented generally transversely to the plate (three in Figure 2) exceeds by one the number for u (two in Figure 2).

4.2. LONGITUDINAL MODES

Also in Figure 1, certain loci grow monotonically with a/b, with the mode labelled (ii) there being representative. This family of modes is analogous to the classical longitudinal vibration modes of a bar in terms of the u–v displacement patterns and the behavior of the

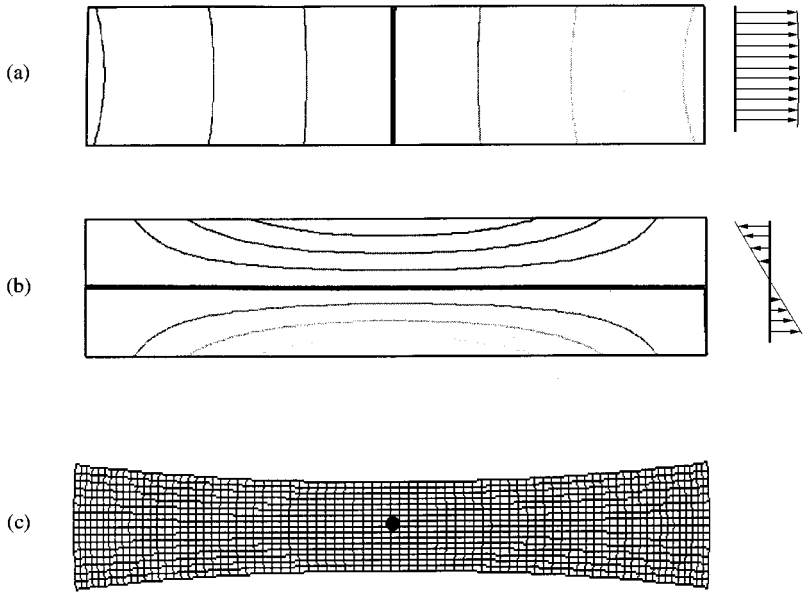

Figure 3. First in-plane longitudinal mode, labelled (ii) in Figure 1, for a free plate at $a/b = 4{\cdot}5$; $\omega = 3{\cdot}13$, symmetric. (a) Longitudinal displacement contour and lateral profile of u, (b) lateral displacement contour and lateral profile of v, and (c) deformed shape with "●" notation signifying nodal points. The nodal lines in (a) and (b) are highlighted in bold.

TABLE 4

Comparison of the present predicted non-dimensional natural frequencies ω^*, and estimates of them as obtained from the first two modes of the classical beam and rod models; free boundary

Free mode	$a/b = 5$			$a/b = 10$		
	ω^*	Beam/rod	Difference (%)	ω^*	Beam/rod	Difference (%)
Beam 1	1·12	1·20	7	0·60	0·61	1
Beam 2	2·63	3·32	21	1·60	1·68	5
Rod 1	3·11	3·03	3	3·14	3·03	4
Rod 2	6·17	5·98	3	6·25	5·98	10

natural frequencies at larger a/b. Shown in Figure 3, mode (ii) is the lowest of this class with motion occurring primarily along the plate's longitudinal axis, and it has reflective symmetry in u relative to the $y = 0$ axis. The u displacement profile shown in Figure 3(a) is nearly constant across the plate's width, and v varies in a substantially linear manner in y. The nth mode of this class has n nodal points that lie on the plate's longitudinal centerline, so that in the nomenclature used here, these modes are also classified as being of first order. Surrounding each node, the plate undergoes local extension or contraction, with the directions alternating at each successive node. In terms of the u and v displacement contours for this class, the number of nodal lines for u oriented generally transversely (one in Figure 3) exceeds by one the number for v (zero in Figure 3).

As the plate's aspect ratio grows, frequencies of modes in this class approach those calculated on the basis of the longitudinal rod model. The circular natural frequency decreases as $1/a$. The non-dimensional frequency as used here is independent of a/b, and

takes on the values $n\pi\sqrt{1-\nu^2}(n = 1, 2, \ldots)$ as denoted by the arrows on the ordinate in Figure 1. At $a/b = 10$, for instance, the frequencies in Figure 1 predicted for the first three modes on the basis of the classical and plane stress models differ by some 5%, namely the multiplicative factor $\sqrt{1-\nu^2}$. For these lower modes, the classical theory slightly underestimates the frequencies to the extent that lateral Poisson contraction/expansion is neglected. At $a/b = 5{\cdot}0$ and $10{\cdot}0$, Table 4 compares predictions of the plane stress model with frequency estimates as obtained from the classical beam and rod models for corresponding modes. At $a/b = 5$, the natural frequency $\omega^* = 1{\cdot}12$ for the lowest bending mode is estimated within some 7% by the classical theory, but the error grows to 21% when the second mode is considered. Similarly, at $a/b = 10$, the classical model estimates the first two longitudinal modes to accuracies of 4 and 10% respectively.

4.3. TWISTING AND HIGHER ORDER MODES

Figure 4 depicts a mode which exists in a region between adjacent veerings of the bending mode loci in Figure 1. In those regions, the frequencies increase steeply with aspect ratio, and this first order mode is identified as mode (iii) in Figure 1. This mode differs from a classical bending mode to the extent that while material particles in the vicinity of a nodal point in each case experience local rotation, here u and v are comparable in magnitude. The transverse profiles for u and v are shown in Figures 4(a, b), where v has substantial cross-plate variation.

The steeper loci in Figure 1 correspond to higher order modes which have nodal points both on and off the plate's longitudinal centerline, and which are not predicted by the classical one-dimensional theories. Examples of certain higher order symmetric and

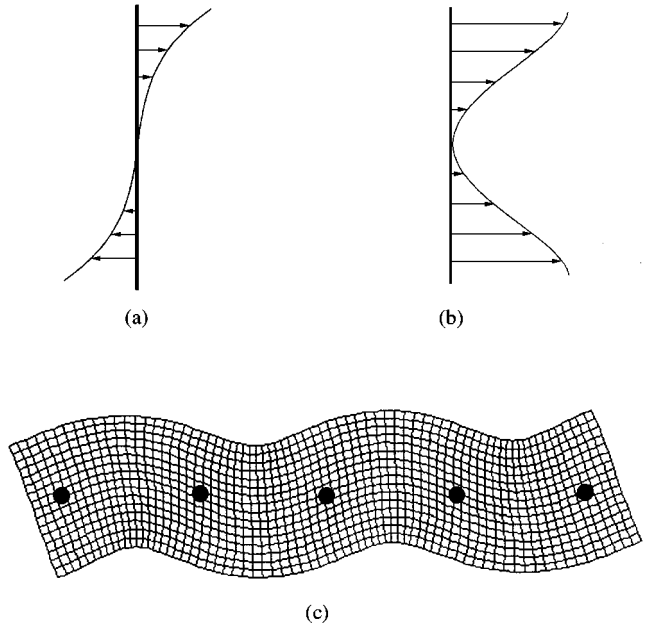

Figure 4. In-plane twisting mode, labelled (iii) in Figure 1, at $a/b = 4{\cdot}5$; $\omega = 8{\cdot}26$. (a) Lateral profile of u, (b) lateral profile of v, and (c) deformed shape with "●" notation signifying nodal points.

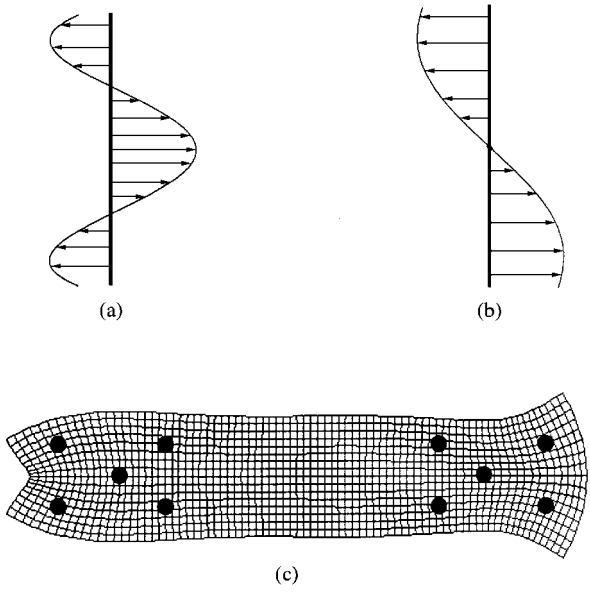

Figure 5. Second order symmetric mode at $a/b = 4{\cdot}5$ for a free plate; $\omega = 13{\cdot}9$. (a) Lateral profile of u, (b) lateral profile of v, and (c) deformed shape with "●" notation signifying nodal points.

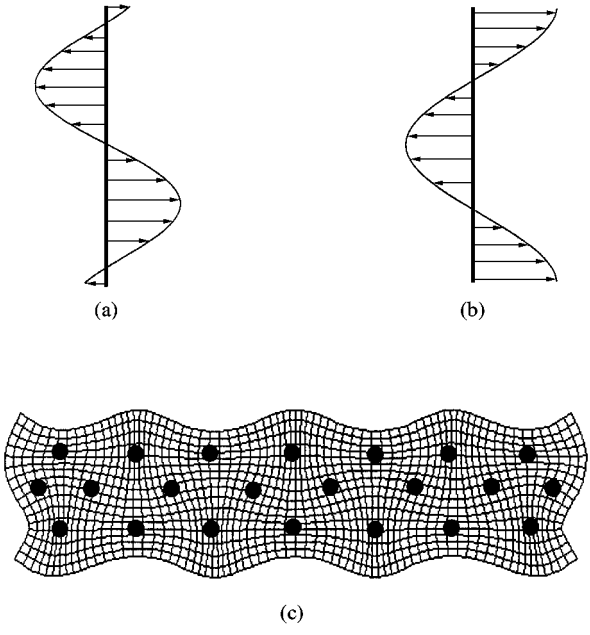

Figure 6. Second order antisymmetric mode at $a/b = 4{\cdot}5$ for a free plate; $\omega = 23{\cdot}3$. (a) Lateral profile of u, (b) lateral profile of v, and (c) deformed shape with "●" notation signifying nodal points.

antisymmetric modes are shown in Figures 5 and 6, respectively, at $a/b = 4{\cdot}5$ and above the frequency range depicted in Figure 1. Qualitatively, these higher order modes present some aspects of the displacement patterns in the bending, longitudinal, and twisting modes. The mode of Figure 5, for instance, exhibits a rod-like displacement pattern along the centerline,

but the material surrounding off-axis nodes experiences local rotation. In Figures 5 and 6, the cross-plate u and v profiles have greater numbers of nodes in the transverse direction relative to those present in the classical modes.

5. CONSTRAINED–FREE BOUNDARY

In this case, edges $x = \pm a/2$ are constrained with $u = v = 0$, but edges $y = \pm b/2$ are free. Figure 7 shows the plate's in-plane frequency spectrum as the aspect ratio is varied over the range $1 \leqslant a/b \leqslant 10$. Also shown in Figure 7 are the asymptotic frequency values predicted on the basis of the classical strength of materials theories for bending (dashed line type; decreasing with $\sqrt{a/b}$) and longitudinal (arrows on ordinate; multiples of π) motions. Table 5 shows the predictions of the plane stress model and of the classical strength of materials rod and beam theories at $a/b = 5{\cdot}0$ and $10{\cdot}0$.

Groups of loci having similar trends with a/b correspond to distinct families of modes. The class of antisymmetric modes that converges with increasing aspect ratio to the classical bending loci is termed the first order bending mode set. Likewise, the symmetric modes which approach the predictions of the longitudinal vibration model at large aspect ratios are termed the first order longitudinal rod modes. Examples of each are denoted in Figure 7 by modes (iv) and (v), respectively, and the mode labelled (vi) is termed an in-plane twisting mode. The higher order modes exhibit displacement behavior similar to that present for

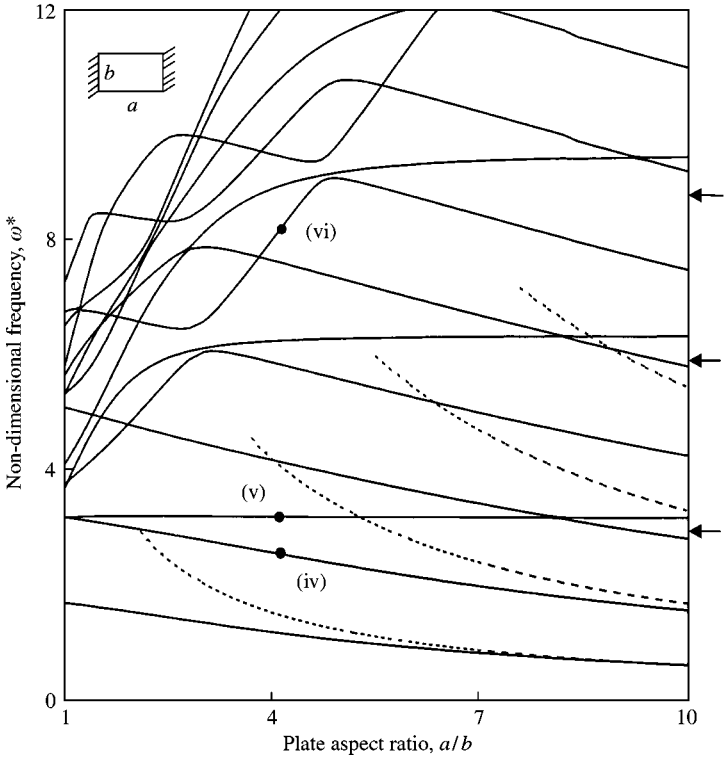

Figure 7. Non-dimensional frequency spectrum for in-plane vibration of a constrained–free plate as a function of aspect ratio (solid line type). For comparison at larger aspect ratios, the frequencies predicted on the basis of the traditional beam bending (dashed line type) and longitudinal rod (arrows on ordinate) theories are also shown.

TABLE 5

Comparison of the present predicted non-dimensional natural frequencies ω^*, and estimates of them as obtained from the first two modes of the classical beam and rod models; constrained–free boundary

Constrained–Free mode	$a/b = 5$			$a/b = 10$		
	ω^*	Beam/rod	Difference (%)	ω^*	Beam/rod	Difference (%)
Beam 1	1·02	1·22	16	0·61	0·61	—
Beam 2	2·55	3·33	23	1·54	1·70	9
Rod 1	2·35	2·18	8	2·18	2·38	9
Rod 2	4·70	4·41	7	4·42	4·73	7

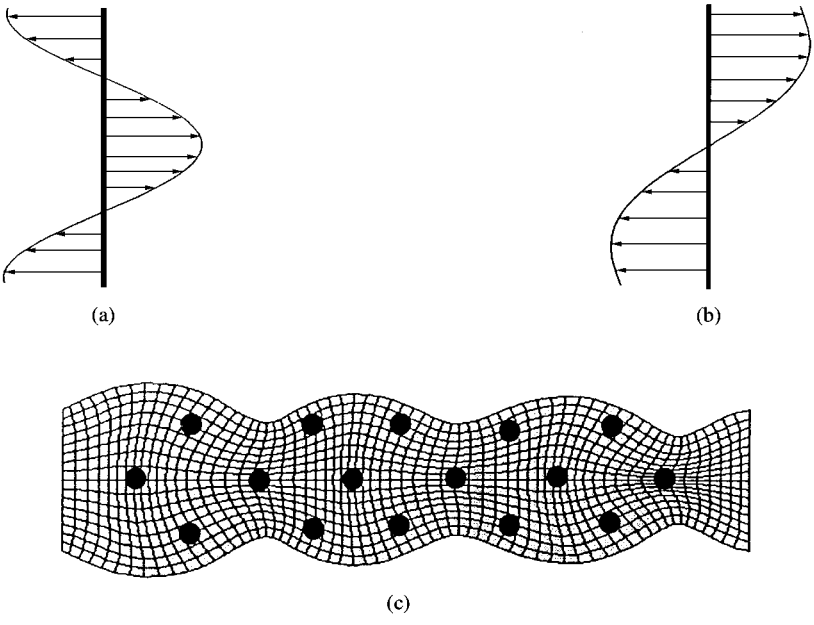

Figure 8. Second order symmetric mode at $a/b = 4$ for a constrained–free plate; $\omega = 13{\cdot}0$. (a) Lateral profile of u, (b) lateral profile of v, and (c) deformed shape with "●" notation signifying nodal points.

a free plate, with the exception of the number of nodes as determined by the transverse edge constraint. Figures 8 and 9 depict two representative higher order modes which have nodal points on, as well as off, the plate's axis. In Figure 8, the u displacement field has two nodal points across the plate's width, while v has one; the values are three and two, respectively, for the mode shown in Figure 9.

6. CONSTRAINED BOUNDARY

The third case examined is that in which all edges of the plate are constrained against u–v displacement, and that spectrum is shown in Figure 10. As in the previous cases, there exist classes of modes which follow the behavior of the first order bending and longitudinal

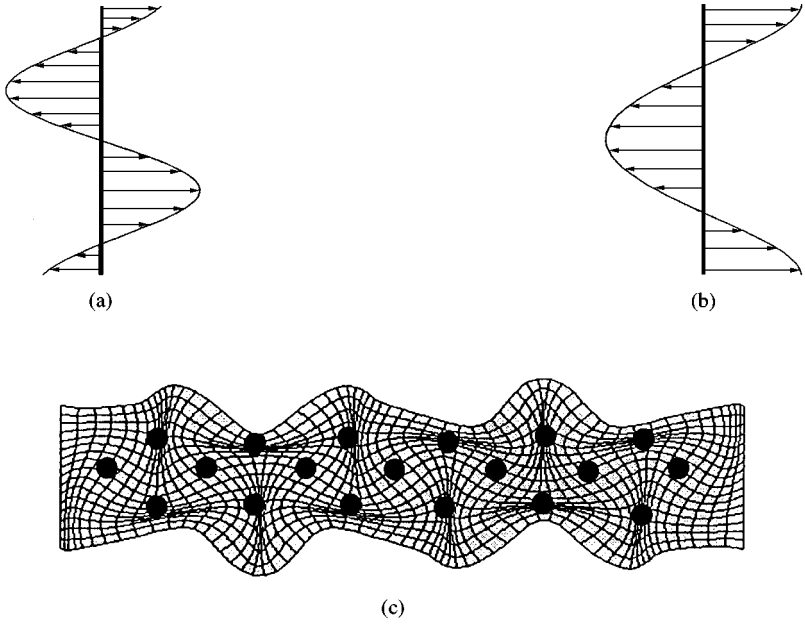

Figure 9. Second order antisymmetric mode at $a/b = 4$ for a constrained–free plate; $\omega = 19{\cdot}5$. (a) Lateral profile of u, (b) lateral profile of v, and (c) deformed shape with "●" notation signifying nodal points.

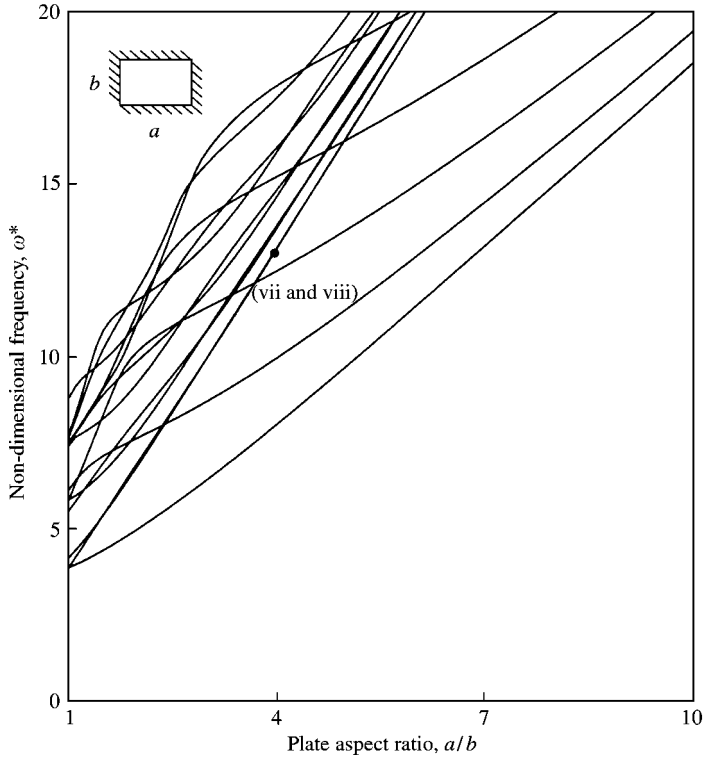

Figure 10. Non-dimensional frequency spectrum for in-plane vibration of a constrained plate as a function of aspect ratio. The nearly repeated frequencies of modes (vii) and (viii), depicted in Figures 11 and 12, are indicated by the "●" notation.

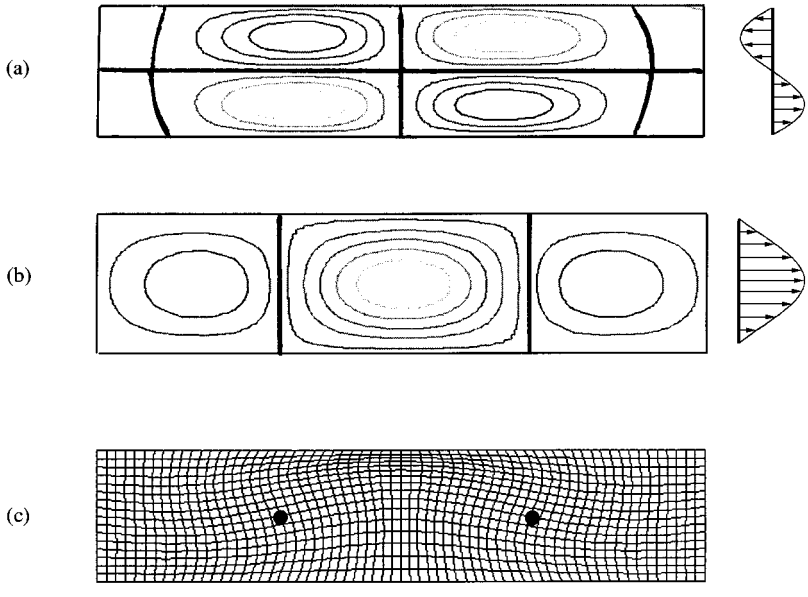

Figure 11. First order antisymmetric in-plane mode, labelled (vii) in Figure 10, for a constrained plate at $a/b = 4{\cdot}75$; $\omega = 14{\cdot}70$. (a) Longitudinal displacement contour and lateral profile of u, (b) lateral displacement contour and lateral profile of v, and (c) deformed shape with "●" notation signifying nodal points. The nodal lines in (a) and (b) are highlighted in bold.

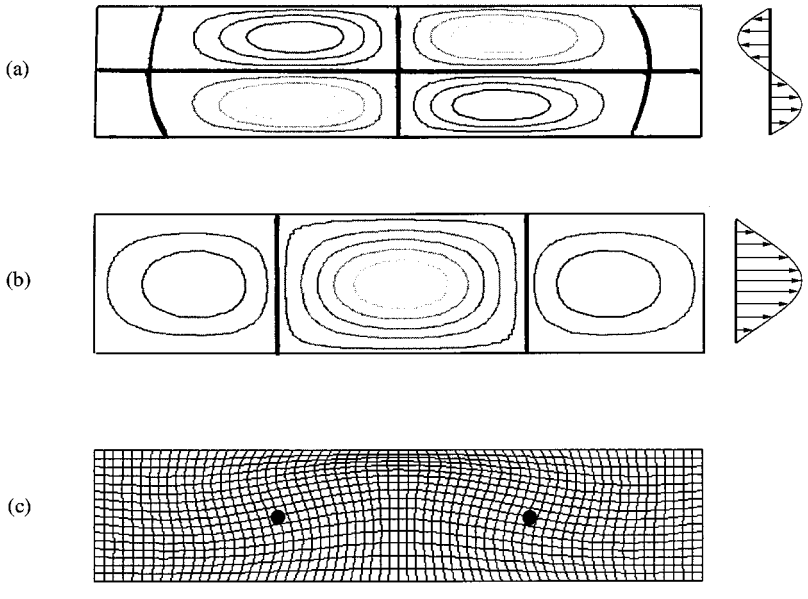

Figure 12. First order antisymmetric in-plane mode, labelled (vii) in Figure 10, for a constrained plate at $a/b = 4{\cdot}75$; $\omega = 14{\cdot}72$. This mode converges in frequency with mode (vii) as the aspect ratio increases. (a) Longitudinal displacement contour and lateral profile of u, (b) lateral displacement contour and lateral profile of v, and (c) deformed shape with "●" notation signifying nodal points. The nodal lines in (a) and (b) are highlighted in bold.

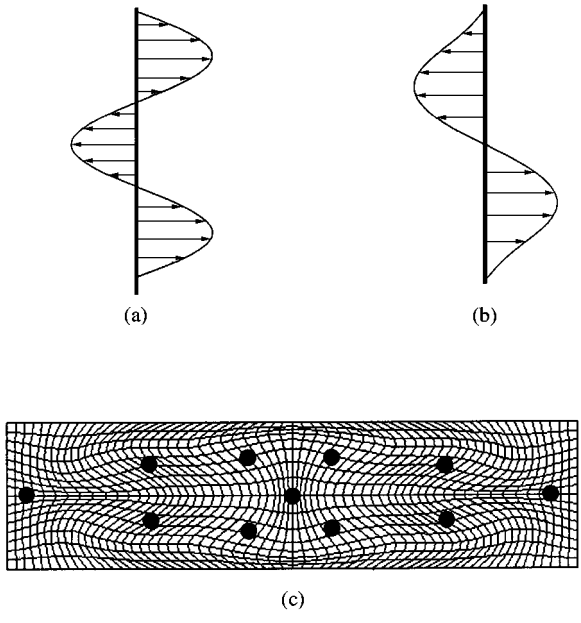

Figure 13. Second order symmetric mode at $a/b = 4{\cdot}0$; $\omega = 22{\cdot}4$. (a) Lateral profile of u, (b) lateral profile of v, and (c) deformed shape with "●" notation signifying nodal points.

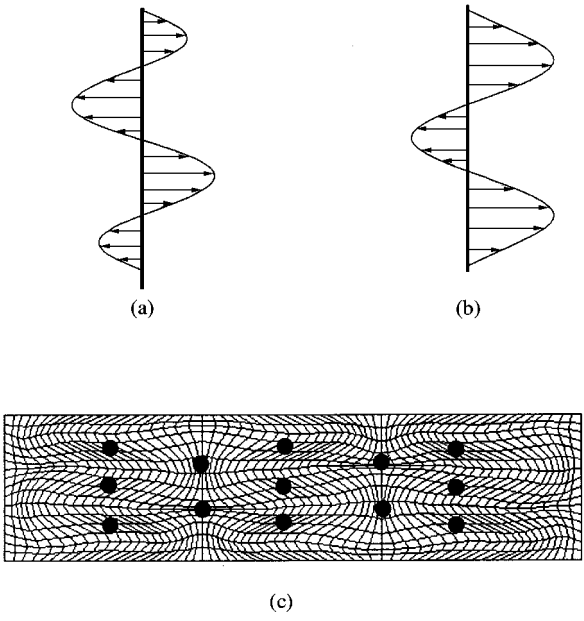

Figure 14. Second order antisymmetric mode at $a/b = 4{\cdot}0$; $\omega = 29{\cdot}5$. (a) Lateral profile of u, (b) lateral profile of v, and (c) deformed shape with "●" notation signifying nodal points.

modes as the constraints along the $y = \pm b/2$ edges are relaxed, but no classical theories exist in this case for the purpose of comparisons.

As the aspect ratio increases, the natural frequencies likewise increase monotonically, unlike the trends present for the first order bending and longitudinal modes with either free

or constrained–free boundaries. At higher aspect ratios, the first order symmetric modes (namely, those having displacement pattern analogous to classical longitudinal rod modes) have the lowest natural frequencies. With increasing a/b, the constraint along $y = \pm b/2$ adds stiffness to each class of modes. Further, pairs of loci, which for small a/b are close but distinguishable in frequency, become asymptotically close in Figure 10 as the aspect ratio grows. Such convergent behavior does not occur for the two other sets of boundary conditions that were examined. An example in that regard is the pair of modes (vii) and (viii), which are shown in Figures 11 and 12 at the aspect ratio of 4·75. These modes, having $\omega = 14{\cdot}70$ and 14·72, respectively, form the first pair to coalesec in frequency, and their displacement patterns would perhaps be described as being most similar to bending modes where material adjacent to each node undergoes local rotation. Examples of two higher order modes are shown in Figures 13 and 14 at $a/b = 4{\cdot}0$, where both transverse profiles and displacement contours are shown.

7. SUMMARY

The natural frequencies and mode shapes for in-plane vibration of a plate are examined through Ritz discretization of the Rayleigh quotient for three representative sets of boundary conditions. Parameter studies over a range of aspect ratios highlight different classes of modes, the lower of which in some cases correspond to the traditional bending and longitudinal vibration theories. The parameter studies in aspect ratio a/b are useful to judge the geometries for which the classical theories can be applied to acceptable levels of accuracy, at least for the lower in-plane modes with free or constrained–free conditions. For instance, at $a/b = 5{\cdot}0$ for a constrained–free plate, the strength-of-materials theories predict the first bending and longitudinal modes to within accuracies of 16 and 8%. Aside from the continuous transition or "morphing" of modes with aspect ratio, other results include the identification of several different classes of modes based on symmetry and the character of displacement patterns near nodal points, and the description of certain higher order modes that are not predicted on the basis of the classical models.

ACKNOWLEDGMENT

This work was supported by the National Science Foundation and the authors' group of industrial sponsors.

REFERENCES

1. K. N. HANDA 1972 *Journal of Sound and Vibration* **21**, 169–180. Analysis of in-plane vibration of shear walls by a finite element method.
2. B. OVUNC 1977 *Computers and Structures* **8**, 723–731. In-plane vibration of plates by continuous mass matrix method.
3. Y. KOBAYASHI, G. YAMADA and S. HONMA 1988 *Journal of Sound and Vibration* **126**, 545–549. In-plane vibration of point-supported rectangular plates.
4. K. M. LIEW, K. C. HUNG and M. K. LIM 1993 *International Journal of Solids and Structures* **30**, 3357–3379. A continuum three-dimensional vibration analysis of thick rectangular plates.
5. K. M. LIEW, K. C. HUNG and M. K. LIM 1994 *International Journal of Solids and Structures* **31**, 3233–3247. Three-dimensional vibration of rectangular plates: variance of simple support conditions and influence of in-plane inertia.
6. K. M. LIEW, K. C. HUNG and M. K. LIM 1995 *Journal of Sound and Vibration* **182**, 709–727. Three-dimensional vibration of rectangular plates: effects of thickness and edge constraints.

7. K. M. LIEW, K. C. HUNG and M. K. LIM 1995 *Journal of Applied Mechanics* **62**, 159–165. Free vibration studies on stress-free three-dimensional elastic solids.
8. N. S. BARDELL R. S. LANGLEY and J. M. DUNSDON 1996 *Journal of Sound and Vibration* **191**, 459–467. On the free in-plane vibration of isotropic rectangular plates.
9. D. LARSSON 1997 *Experimental Mechanics* **37**, 339–343. In-plane modal testing of a free isotropic rectangular plate.